Bunching and Immobilization of Ionic Liquids in Nanoporous Metal–Organic Framework

Anemar Bruno Kanj,[†,§] Rupal Verma,[†,§] Modan Liu,[‡,§] Julian Helfferich,[‡] Wolfgang Wenzel,[*,‡] and Lars Heinke[*,†]

[†]Karlsruhe Institute of Technology (KIT), Institute of Functional Interfaces (IFG), Hermann von Helmholtz Platz 1, 76344 Eggenstein Leopoldshafen, Germany

[‡]Karlsruhe Institute of Technology (KIT), Institute of Nanotechnology (INT), Hermann von Helmholtz Platz 1, 76344 Eggenstein Leopoldshafen, Germany

Supporting Information

ABSTRACT: Room temperature ionic liquids (ILs) are a unique, novel class of designer solvents and materials with exclusive properties, attracting substantial attention in fields like energy storage and supercapacitors as well as in ion based signal processing and electronics. For most applications, ILs need to be incorporated or embedded in solid materials like porous hosts. We investigate the dynamic structure of ILs embedded in well defined pores of metal–organic frameworks (MOFs). The experimental data combined with molecular dynamics simulations unveil astonishing dynamic properties of the IL in the MOF nanoconfinement. At low IL loadings, the ions drift in the pores along the electric field, whereas at high IL loadings, collective field induced interactions of the cations and anions lead to blocking the transport, thus suppressing the ionic mobility and tremendously decreasing the conductivity. The mutual pore blockage causes immobilized ions in the pores, resulting in a highly inhomogeneous IL density and bunched up ions at the clogged pores. These results provide novel molecular level insights into the dynamics of ILs in nanoconfinement, significantly enhancing the tunability of IL material properties.

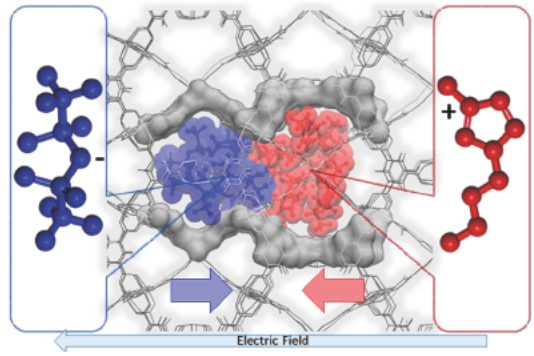

KEYWORDS: *Ionic liquid, nanoconfinement, metal–organic framework, HKUST 1, ion bunching*

Room temperature ionic liquids (ILs) are molten salts of organic cationic and anionic molecules. Their outstanding physical and chemical properties, such as negligible vapor pressure, nonflammability, thermal stability, and solubility of different materials, make them perfectly suited for various applications.[1] The cations and anions can be exchanged, resulting in a virtually unlimited number of IL structures with tunable properties.[2] Because they can be recovered and recycled, ILs are extensively applied as catalysts and as alternative solvents in homogeneous catalysis and extraction.[3,4] Moreover, these designer liquids are suitable for electro chemical applications[5,6] and are used as electrolytes in supercapacitors[7,8] and microsupercapacitors,[9] in solar cells[10] and fuel cells[11] as well as in lithium batteries[12] and other advanced battery technologies.[6] In most of these cutting edge applications, the fluid nature of ILs is unfavorable and a solid like material is desirable.[13] This can be achieved by confining ILs in small geometries, resulting in porous materials filled with IL.[14,15] Common porous hosts for ILs are nanoporous carbons and carbon nanotubes as well as nanoporous silica.[7,14,15] The confinement in crystalline metal–organic frameworks (MOFs), a novel class of tunable nanoporous hybrid materials composed of metal ions connected by organic linker molecules,[16,17] had also been demonstrated recently.[8,18,19] The electric aspects of the IL materials are particularly interesting and enable various applications in the field of iontronics, an interdisciplinary research field bridging electronics and ionics based on electrochemistry, solid state physics, electronic engineering, and biological sciences.[13,20] In addition to the previously mentioned usages, iontronics with ILs may improve applications in chemical sensing, thermoelectrics, transistors, and light sources and enable printable electronics.[13] The investigation of ILs confined in small geometry demonstrated unexpected structural properties, significantly deviating from the bulk IL properties. For instance, the confinement of an IL between two interfaces may result in unique lubricant properties.[21,22] Thermodynamic characteristics such as the melting point or solubility may also be influenced by the confinement in nanoporous materials like amorphous carbons[14,15] and crystalline MOFs.[23] Moreover, it was found that confining ILs in small, sub nanometer sized pores in

supercapacitors results in particularly high capacitances and energy densities.[24,25] The confinement in such nanopores may also exhibit a partial breaking of the Coulombic ordering.[26] In addition to the astonishing insights into the static properties, theoretical calculations predicted staggering dynamic properties of IL in the nanoconfinement of slit pores.[27] However, the dynamic aspects, which are crucial for the applications such as the charging and discharging processes of supercapacitors and batteries, have hardly been explored to date.

Here we investigate the conduction properties of IL of type 1 butyl 3 methylimidazolium bis(trifluoromethylsulfonyl) amide, referred to as [BMIM][NTf_2] (or [BMIM][TFSA]),[28] in regular pores of relatively rigid, crystalline MOFs[16,17] of type HKUST 1[29] (Figure 1). Both components are among the most

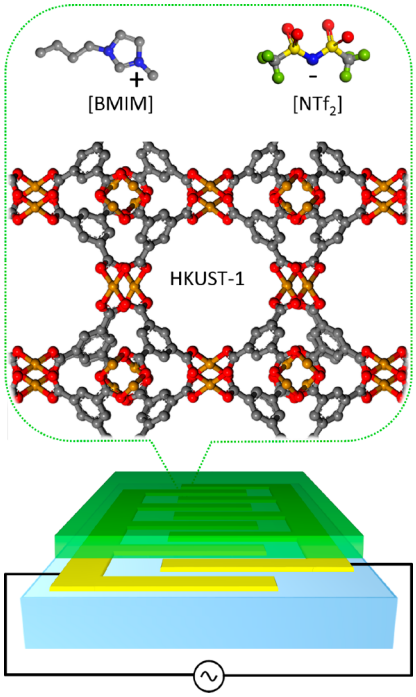

Figure 1. [BMIM][NTf_2] ionic liquid confined in regular nanopores of HKUST 1 MOF. The HKUST 1 has a relatively rigid, face centered cubic structure with a unit cells size of $(2.6\ nm)^3$ and a 3D pore system with pores of ~1.3 nm diameter connected by pore windows of 0.9 nm diameter. The size of the [BMIM] cations and [NTf_2] anions is approximately 0.5 nm × 0.6 nm × 1.0 nm and 0.5 nm × 0.4 nm × 1.0 nm, respectively. To determine the ohmic resistance of IL@MOF, HKUST 1 MOF thin films were grown on interdigitated gold substrates and investigated via impedance spectroscopy. The color code for the atoms is C, gray; O, red; Cu, orange; N, blue; F, green; S, yellow. H is not shown.

popular representatives of each material class. To avoid excess IL outside the MOF pores, we use MOFs in form of well defined, dense films prepared by layer by layer (lbl) deposition, also referred to as SURMOFs.[30,31] In contrast with the bulk IL, the IL density in the porous medium can be varied. Similar to the dynamics of (conventional) fluids in nanoporous materials, where it is commonly distinguished between a low concentration region with insignificant guest−guest interaction (often referred to as the Henry region) and a high concentration region with strong guest−guest interaction, both in addition to the guest−host interaction,[32] we anticipate two regimes for the ionic transport in the porous structure. For low ion concentrations, by analogy to the constant diffusion coefficient in the Henry region, we expect a constant molar conductivity (or mobility) because the individual ions do not interact. As the ion concentration increases in the porous medium, ion−ion interaction effects may dominate. We find that the ion interaction leads to a decrease in the mobility because the cations and anions, moving in opposite directions, obstruct each other. In addition to these findings, our experimental data show an additional large drop of IL mobility and ionic conductivity for high pore filling. These data could be rationalized by molecular dynamics (MD) simulations, which unveil a novel molecular mechanism, based on a new type of collective density fluctuation. This density fluctuation leads to an inhomogeneous distribution of the ions in the MOF, which we term "bunching". The ion bunching is correlated to transient mutual pore blockage of the cations and anions in the rigid pores of the host MOF. The pore blockage results in immobilized and jammed IL in the pore system, thus clogging the conduction pathways and resulting in a decrease in the conductivity by many orders of magnitude.

Results and Discussion. The HKUST 1 MOF films were loaded with IL from IL−acetonitrile solutions of various concentrations. Acetonitrile was chosen as the solvent because it is fully mixable with [BMIM][NTf_2] and its conductivity is very small, and thus the measured conductivity can be solely attributed to the IL. In addition, acetonitrile is very volatile at room temperature and evaporates very fast from the MOF pores. The X ray diffractogram (XRD) (Supporting Information (SI) 1) shows that the HKUST 1 SURMOF is grown in a (100) orientation on the interdigitated electrode substrate. Upon IL loading, the XRD form factor changes, which is a clear indication of the loading of the IL in the MOF pores. Upon rinsing the IL loaded sample with ethanol for 20 min, a diffractogram similar to the diffractogram of the pristine sample is obtained. The infrared (IR) spectra of the sample, with and without IL loading, are shown in SI 2. The data show that the acetonitrile evaporates, leaving pure IL in the MOF pores. The amount of the IL uptake by the SURMOF from acetonitrile solutions with different IL concentrations was quantified by using a quartz crystal microbalance[33,34] as well as by energy dispersive X ray (EDX) spectroscopy (SI 3). The IL loading in the MOF pores is essentially proportional to the IL concentration in the solution, and a maximum pore filling of ~18.6 ± 0.7 [BMIM][NTf_2] IL pairs per HKUST 1 MOF unit cell (i.e., ~19 IL per unit cell (uc)) was estimated.

The conductivity of the IL@MOF samples was measured by impedance spectroscopy. Typical Nyquist plots of the same sample with different IL pore fillings are shown in Figure 2. Because the impedance spectra of the empty HKUST 1 MOF show only a capacitive component of the impedance, we conservatively estimate the ohmic resistance of the empty MOF to be 10^{12} Ω, which is approximately the highest impedance measurable by our setup. Thus on the basis of the thickness of ~0.25 μm, determined by scanning electron microscopy, which also shows a homogeneous film morphology (see SI 4), the conductivity of the empty MOF is $<5 \times 10^{-11}$ S m^{-1}. This is in agreement with values reported in the literature.[35] By filling the MOF pores with the IL, the conductivity of the sample increases by many orders of magnitude in comparison with the empty MOF.

The molar conductivities of the IL embedded in the HKUST 1 SURMOF film are shown in Figure 3a for different IL loadings. At small loadings, that is, with 20% IL pore

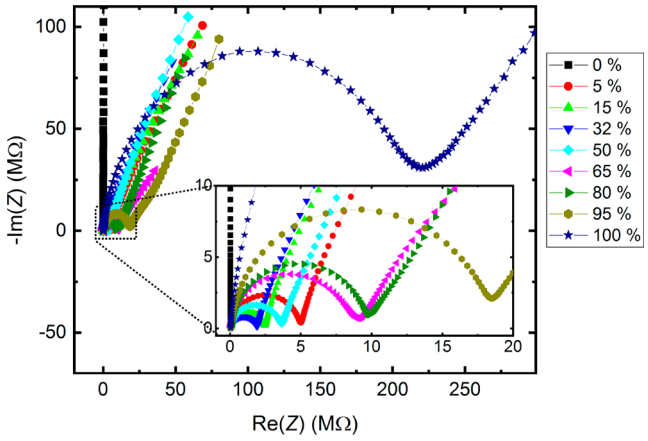

Figure 2. Nyquist plots of the impedance of the HKUST 1 MOF film with various fillings of ionic liquid. The [BMIM][NTf_2] IL loading is given in the legend on the right hand side. Except for the sample without IL, where only a capacitive resistance was measured, all impedance spectra could be described with the Randles circuit model.[36] The frequency range is 0.5 Hz to 5 MHz.

loading and less, the molar conductivity has a constant value of (45 ± 20) nS m^2 mol^{-1}. This value is roughly three orders of magnitude smaller than the conductivity of pure, bulk [BMIM][NTf_2], which is ~1.0 × 10^{-4} S m^2 mol^{-1} at room temperature.[37] For pore loadings which are >20%, the molar conductivity decreases approximately exponentially (i.e., linear on the log scale) with increasing IL loading. At a pore loading of 95%, a molar conductivity of (0.7 ± 0.4) nS m^2 mol^{-1} is obtained. This means by increasing the loading from 20 to 95%, the molar conductivity decreases by approximately two orders of magnitude. By further increasing the pore loading from 95 to 100%, that is, to the maximum pore loading, the molar conductivity decreases by one order of magnitude to about (0.07 ± 0.04) nS m^2 mol^{-1}.

To investigate the microscopic origins and improve the understanding of this surprising drop in conductivity, we have employed MD simulations using a fully atomistic model of the MOF and the guest molecules. The fully atomistic model also contains mechanic friction caused by guest−guest and guest−host interactions. In the MD simulations, a maximum pore filling of 19 IL per uc was determined by a packing algorithm, which is in very good agreement with the experimental value. The concentration dependence of the mobility for E = 5.0 and 7.5 V nm^{-1} is shown in Figure 3b (additional data in the Figure SI6). We find that the conductivity varies significantly over the considered pore loading range. For a wide range of loading, up to 17 IL per uc, we find a near exponential decrease in the conductivity as a function of loading, irrespective of the specific value of the field. If we increase the loading further to 19 IL per uc, then we find an additional drop of the conductivity below the trend line by a factor of 2.5 and 2 for E = 5.0 and 7.5 V nm^{-1}, respectively. Thus the experimentally determined features of the IL conduction in the MOF pores were reproduced by MD simulations.

Detailed inspections of the MD simulations enable a more detailed analysis and comprehension of the observed phenomenon. Videos of the MD of the IL in the MOF pores are shown in SI 9; snapshots of the simulations and a statistical evaluation are shown in Figure 4. The MD data show that at low IL loadings, where the percentage of free volume is large (Figure SI10), the anions and cations drift along the electric field in opposite directions without significant interaction. Because both ions, [BMIM] and [NTf_2], are singly charged and occur with the same average concentration, the electric forces on each ion have the same value but in opposite directions. At medium loadings (Figure 4a), anions and cations are forced to share the same pore windows at the same time. Because of the MOF pore size, which does not allow the simultaneous passage of both ions, the opposite drift direction of the ions leads to a mutual blockage and a transient jam of the pore windows. However, in all snapshots of the simulations, the ions are essentially uniformly distributed across the pore volume of the simulations cell (Figure 4b). We note that the experimentally observed constant conductivity (and mobility) at very low loading (see Figure 3a) is difficult to observe in the MD simulations. This may have several reasons: First, the applied electric field strengths are very high, which accelerates the ions faster than in the experiments. Second, the MOF in the simulation is perfectly aligned with the field, which also reduces the scattering of the ions during the transport.

At high loading with only a small percentage of free volume, we observe an inhomogeneous overall density of ions in the

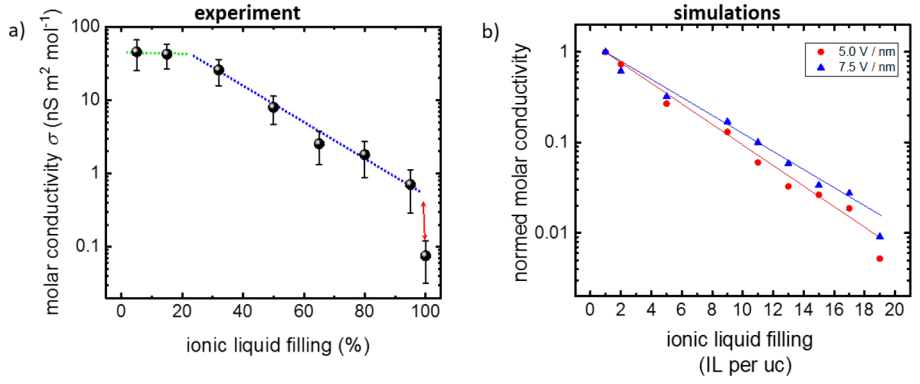

Figure 3. Molar conductivity of [BMIM][NTf_2] ionic liquid in HKUST 1 with different pore fillings. (a) Experimentally determined mean values with the standard deviation as error bars. The ohmic resistances as a function of pore loadings are shown in Figure SI5. (b) Molar conductivity determined from molecular dynamics simulations with different electric fields, E; see the inset. The data are normalized to the value at a loading of 1 IL per uc. The thin lines represent the trend lines of the data up to 17 IL per uc. In addition to the kinetics based analysis (b), the simulation data were analyzed using a transient time correlation function,[38] resulting in essentially identical conductivities (Figure S11). The absolute values of the simulated conductivity are shown in Figure S12.

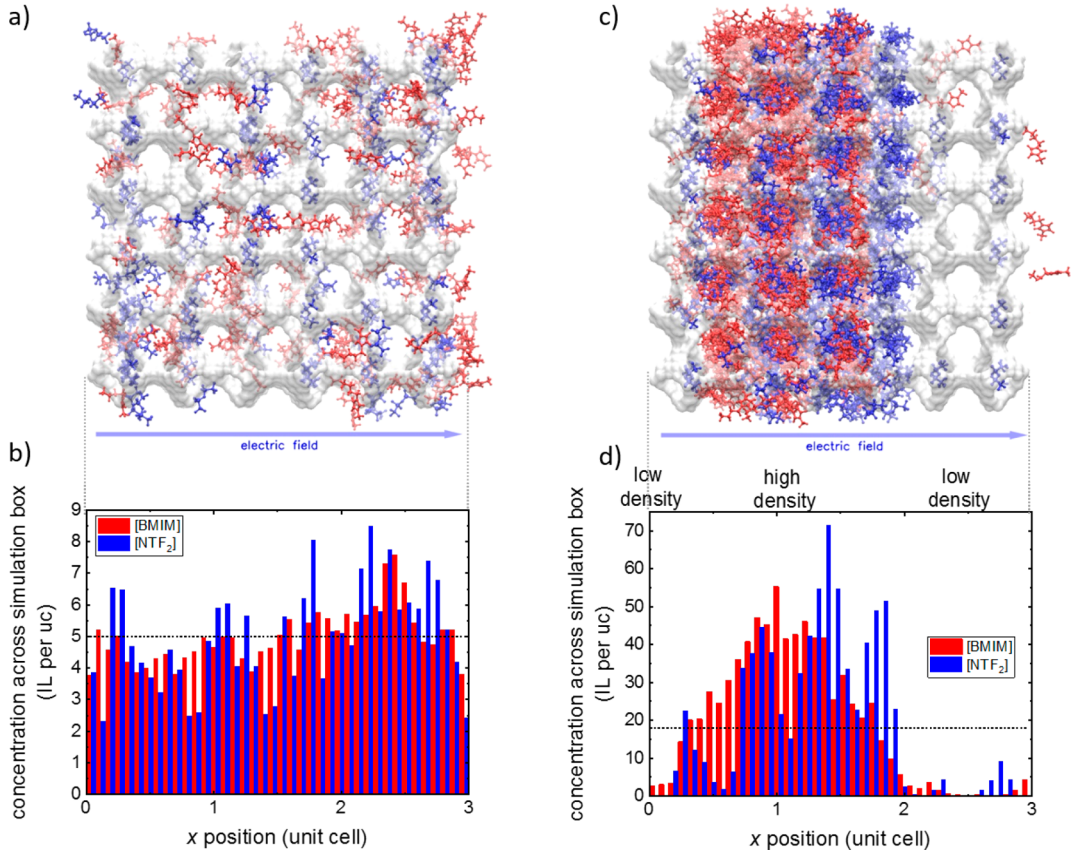

Figure 4. Detailed inspection of MD simulation data. Snapshots of the simulation box with (a) 5 and (c) 19 IL per uc. (b,d) Density distributions of [BMIM] cations (red) and [NTf_2] anions (blue) of the snapshots shown in panels a and c averaged over a time interval of 0.2 ns. The vertical dotted lines between the panels illustrate the position of the histogram of the IL density. The horizontal dotted lines in panels b and d represent the average density. The electric field of 7.5 V nm^{-1} is horizontally oriented, so that the cations drift to the right and anions drift to the left. Whereas the void volume in panel a is ~38%, with small fluctuations, the void volume in panel c is only 5.2% in the high density region and ~43% in the low density region.

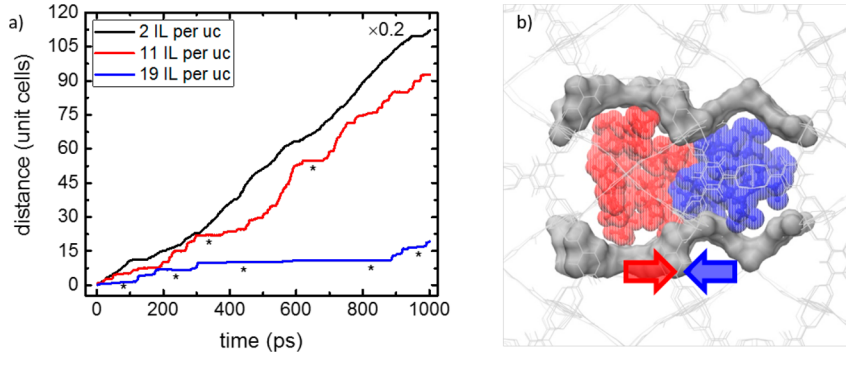

Figure 5. (a) Typical trajectories of single [BMIM] cation with an average concentration of 2 (black), 11 (red), and 19 (blue) IL per uc. Note that the distance of the black trajectory is divided by 5 to enable a comparison in one plot. The plateaus, showing the transient immobilization, labeled with asterisks, align well with the positions of the pore windows. The distance is plotted in units of unit cells, corresponding to 2.6 nm. The electric field is 7.5 V nm^{-1}. (b) Sketch of a blocked MOF pore where [BMIM] cations (blue) and [NTf_2] anions (red) try to pass simultaneously. The atoms of the MOF in close proximity to the confined IL are plotted gray; the rest of the MOF structure is indicated by thin gray lines. The electric field is horizontally oriented so that the cations drift to the right and the anions to the left.

MOF (Figure 4c), comprising high and low density regions. Analyzing snapshots of the inhomogeneous ion distribution at an average loading of 19 IL per uc (Figure 4d), we find that cation and anion densities develop peaks to the left hand side and to the right hand side of a pore window, respectively. The [NTf_2] anions exhibit a more pronounced density inhomoge neity than [BMIM] cations, presumably a result of their lower diffusivity due to their significantly larger mass and size. It is remarkable that the external electric field results in MD where the initial homogeneous distribution of the IL becomes strongly inhomogeneous, a phenomenon we call "bunching" of the IL in the MOF pores. A video of the development of the IL bunching is also present in the SI (see SI9). We stress that the IL inhomogeneities and the bunching develop in a

homogeneous MOF lattice with a periodic (defect free) arrangement of pores and pore windows in combination with a homogeneous external electric field. The position of the high density region moves randomly across the simulation box, and the magnitude of the density fluctuation varies with time. In the high density region, the IL density at the clogged pores is significantly larger than the average density. In Figure 4d, the density close to the clogged pore window is approximately two times larger than the average density and approximately five times larger than that in the low density region. This is in contrast with low IL loading, for example, 5 IL per uc, where the distributions of both ions remain essentially homogeneous without perceptible pore blocking, jamming, or bunching effects (Figure 4b).

Following the trajectories of single ions enables further insights into the molecular mechanism. At low IL loadings, the ions drift in the direction of the electric fields, and the fast drift, accelerated by the external electric field, is only slowed down by the friction with the host framework. The traveled distance in this regime is nearly proportional to the time, and the drift velocity is roughly constant; see Figure 5a and Figure SI7. At high IL loadings, the trajectory of individual ions can be decomposed into a nearly stationary phase (labeled with asterisks in the Figure 5a), where the ions are immobile, followed by short bursts of movement. During these rather long immobile periods, the ions are stuck in the vicinity of the pores because the density fluctuation has increased the local density to a value much larger than the average density. This effect tends to further slow the ions down locally, which, in turn, amplifies the size of the density fluctuation. After some time, here up to 600 ps, the ion starts drifting again until it gets stuck in the next high density region. Because the density fluctuations also result in low density regions, the ions accelerate after they pass a high density region, which results in a transient character of the phenomenon. A snapshot of a blocked pore is shown in Figure 5b. Anions and cations, with electrostatic forces acting in opposite directions, cannot mutually pass the pore windows, resulting in a clogged pore. At the clogged pore, the free volume is decreased, further decreasing the ion mobility in the area, causing an ion jam and a clogged area.

As a reference, we have also conducted simulations for the bulk IL. In the bulk phase of IL, the external electric field leads to unhindered drifts of the anions and cations in opposite directions. The anions and cations usually drift in separate fiber like pathways in close proximity to each other.[39] This can be seen in the simulations of the bulk IL (SI 8). In the case of IL in MOFs, the MOF structure and the small pore windows of the MOF suppress the formation of cation and anion fibers in close proximity, resulting in completely different dynamics.

Conclusions. The conduction properties and dynamic structure of ILs in well defined confinement of pores of crystalline MOFs have been investigated experimentally and by MD simulations. Whereas the ionic conduction occurs without significant interaction between the ions at low IL loadings in the pores, a tremendous mutual impact of the IL cations and anions occurs at high loadings. Because of the rigid pore structure and the pore window size hindering the simultaneous passage of ions, the cations and anions, traveling in opposite directions when an external electric field is applied, mutually block the pore windows at high concentrations. The pore blockage results in an immobilization of the ions and in an ion jam in the pore system, tremendously decreasing the conductivity of the IL−MOF material. Moreover, the initial homogeneous distribution of the IL in the MOF becomes strongly inhomogeneous, and bunched up ILs at the clogged pores can be observed.

The study using IL embedded in SURMOFs as a well defined model system shows that the ionic conductivity may be increased—counterintuitively—by decreasing the amount of charge carrier. This phenomenon, although it was explored in nanoporous materials with a regular arrangement of pores, is not limited to crystalline materials. These effects also occur in other porous materials with pore windows in the nanometer and subnanometer range such as nanoporous carbons. Once the threshold (of the pore window and/or ion size) for immobilization is known, this effect enables us to control the IL mobility from an essentially immobile and inactive state to a mobile and active state, allowing the adjustment of ionic conductivity, desirable for various biological and sensing applications of iontronics.[13,40,41] The control of the ion mobility also has profound consequences for technical applications of IL@porous materials, for instance, by accelerating the charging and discharging processes of supercapacitors. Thus, instead of using pure IL,[8,24] the kinetics of IL in various nanoporous solids can be improved by using mixtures or solvents with optimized IL concentrations without significantly decreasing the capacitances.

Methods. *SURMOF Synthesis and IL Loading.* The lbl SURMOF synthesis on functional surfaces has been previously discussed in detail.[30,31] The lbl growth process consists of alternately exposing the substrate to the ethanolic solutions of the building units, that is, the metal nodes (here: 0.5 mM copper acetate) and the organic linkers (here: 0.1 mM BTC (benzene 1,3,5 tricarboxylic acid)). Between each immersion step, the samples were cleaned with pure ethanol. The SURMOF samples were prepared in 40 lbl synthesis cycles by using a spray method.[42] The interdigitated gold substrates were treated by UV ozone treatment for 30 min to remove impurities as well as increase the number of OH functional groups and the hydrophilicity. The interdigitated gold electrodes on glass substrates were obtained from DropSens. The total length of the gap between the gold electrodes is 1.68 m, and the gap width is 10 μm.

The HKUST 1 SURMOFs were loaded with the IL by immersing the sample in IL/acetonitrile solutions with an IL ratio of 0, 5, 15, 32, 50, 65, 80, 95, and 100%. The immersion time was 20 min. The temperature was 298 K. After the immersion, the sample was rinsed with acetonitrile for 2 s to remove IL from the outer sample surface, that is, to remove all ILs outside the MOF pores. Subsequently, the sample was dried in a flow of pure nitrogen. This removes the acetonitrile molecules, which are very volatile at room temperature, from the pores. In the gas flow, ILs were not removed from the pores due to their vanishing vapor pressure.

The XRDs (Figure SI1) were measured in out of plane geometry using a Bruker D8 Advance diffractometer equipped with a position sensitive detector in $\theta-2\theta$ geometry. A Cu anode with a wavelength of λ = 0.154 nm was used. The IR spectra (Figure SI2) were recorded with a Fourier transform infrared reflection absorption (FT IRRA) spectrometer (Bruker Vertex 80). The spectra were recorded in grazing incidence reflection mode at an angle of incidence of 80° relative to the surface normal. The IL uptake (Figure SI3) was determined using a quartz crystal microbalance E 4 from Q Sense. Energy dispersive X ray (EDX) spectra were recorded

with a TESCAN VEGA3 scanning electron microscope equipped with a Bruker EDX unit.

Measurement of Electric Conduction Properties. The impedance spectra were measured using a Zurich Instruments MFIA impedance analyzer for a frequency range of 5 MHz to 0.5 Hz. The sample was placed in a homemade cell where the interdigitated gold electrodes on the substrate were contacted in a two probe way. Ion conduction was measured over a distance of 10 μm (corresponding to 3846 unit cell lengths). Because the resistance was determined by impedance spec troscopy, an accumulation of ions at the electrodes could not occur in this experiment. Further details of the setup can be found in ref 43. The electric field on the interdigitated electrode substrates is ~0.1 V μm^{-1}. The cell was purged with pure argon with a flow rate of 10 mL min^{-1}. All experiments were performed at room temperature (298 K). The data (Figure 3) were obtained from two samples where each IL concentration was varied for three cycles (0% → 5% → ... → 95% → 100%). The calculated molar conductivity refers to the [BMIM][NTf_2] IL.

Molecular Dynamic Simulations. For the MD simulations, we adopted the UFF4MOF force field, a fully atomistic force field developed specifically for MOFs.[44,45] For the IL, we used a similarly well established force field.[46] All simulations have been performed using the LAMMPS[47] simulation package. The time step of the simulation was τ = 0.25 fs, and the Nosé−Hoover thermostat[48] and Nosé−Hoover−Andersen barostat[49] were used to model NPT conditions at atmospheric pressure (p = 1 atm) and a temperature of T = 300 K. The initial structure was constructed as a 3 × 3 × 3 supercell from a HKUST 1 unit cell obtained from ref 45, loaded with a varying number of IL molecules using the PACKMOL tool. Starting with this initial structure, we first performed an energy minimization using the conjugate gradient method[50] and then equilibrated the structure during a 1 ns simulation run without an external field. To determine the molecular mobility, we performed simulation runs of 10 ns with an external electric field parallel to the x axis. Because of the limited time scales of MD simulations, an electric field stronger than the electric field applied in the experiments was used in the calculations. Such methods are well established.[51,52] To assess the effect of the stronger field, we performed simulations at E = 2.5, 5.0, 7.5, and 10 V nm^{-1}. The molar conductivity has been determined by measuring the drift velocity of the two types of ions. From the drift velocities, the molar conductivity can be directly determined as $\Lambda_m = E^{-1}F(q_{cation}\langle v\rangle_{cation} + q_{anion}\langle v\rangle_{anion})$, where q is the charge of the ion, $\langle v\rangle$ is the drift velocity, and F is the Faraday constant. In addition to the kinetics based analysis, the simulation data were analyzed using a transient time correlation function (TTCF),[38] Figure S11. Because two independent methods converged to the same kinetics regarding the molar conductivity (TTCF and direct simu lation), we expect the same behavior for smaller electric fields.

ASSOCIATED CONTENT

Supporting Information

The Supporting Information is available free of charge on the ACS Publications website at DOI: 10.1021/acs.nanolett.8b04694.

Experimental data from XRD, IRRAS, QCM, EDX, and SEM and simulation data (PDF)

Video of the simulation data with 5 IL per uc (MPG)

Video of the simulation data with 19 IL per uc (MPG)

Video of the evolution of the pore clogging (MPG)

3D view of a snapshot of the clogged pore (MPG)

AUTHOR INFORMATION

Corresponding Authors

*E mail: Lars.Heinke@kit.edu.

*E mail: Wolfgang.Wenzel@kit.edu

ORCID

Anemar Bruno Kanj: 0000 0001 6385 4634

Lars Heinke: 0000 0002 1439 9695

Author Contributions

§A.B.K., R.V., and M.L. contributed equally. All authors contributed to writing the manuscript and have approved the final version of the manuscript. A.B.K. and R.V. synthesized the samples and performed experiments. M.L., J.H., and W.W. performed the MD simulations. L.H. planned and supervised the experiments and wrote the manuscript.

Notes

The authors declare no competing financial interest.

ACKNOWLEDGMENTS

We gratefully acknowledge funding by the Volkswagen Foundation, the Fonds der Chemischen Industrie, and the German Science Foundation (DFG HE 7036/5). This work was also funded by the SFB 1176 "Molecular Structuring of Soft Matter" (project Q3) and the project MSMEE of the Baden Württemberg Stiftung. This work was performed on the computational resource ForHLR II funded by the Ministry of Science, Research and the Arts Baden Württemberg and DFG ("Deutsche Forschungsgemeinschaft").

REFERENCES

(1) Hallett, J. P.; Welton, T. *Chem. Rev.* **2011**, *111*, 3508−3576.

(2) Plechkova, N. V.; Seddon, K. R. *Chem. Soc. Rev.* **2008**, *37*, 123−150.

(3) Passos, H.; Freire, M. G.; Coutinho, J. A. P. *Green Chem.* **2014**, *16*, 4786−4815.

(4) Steinrück, H. P.; Libuda, J.; Wasserscheid, P.; Cremer, T.; Kolbeck, C.; Laurin, M.; Maier, F.; Sobota, M.; Schulz, P. S.; Stark, M. *Adv. Mater.* **2011**, *23*, 2571−2587.

(5) Armand, M.; Endres, F.; MacFarlane, D. R.; Ohno, H.; Scrosati, B. *Nat. Mater.* **2009**, *8*, 621−629.

(6) MacFarlane, D. R.; Tachikawa, N.; Forsyth, M.; Pringle, J. M.; Howlett, P. C.; Elliott, G. D.; Davis, J. H.; Watanabe, M.; Simon, P.; Angell, C. A. *Energy Environ. Sci.* **2014**, *7*, 232−250.

(7) Simon, P.; Gogotsi, Y. *Nat. Mater.* **2008**, *7*, 845.

(8) Sheberla, D.; Bachman, J. C.; Elias, J. S.; Sun, C. J.; Shao Horn, Y.; Dinca, M. *Nat. Mater.* **2017**, *16*, 220−224.

(9) Kyerematen, N. A.; Brousse, T.; Pech, D. *Nat. Nanotechnol.* **2016**, *12*, 7−15.

(10) Hagfeldt, A.; Boschloo, G.; Sun, L. C.; Kloo, L.; Pettersson, H. *Chem. Rev.* **2010**, *110*, 6595−6663.

(11) de Souza, R. F.; Padilha, J. C.; Goncalves, R. S.; Dupont, J. *Electrochem. Commun.* **2003**, *5*, 728−731.

(12) Bruce, P. G.; Freunberger, S. A.; Hardwick, L. J.; Tarascon, J. M. *Nat. Mater.* **2012**, *11*, 19−29.

(13) Bisri, S. Z.; Shimizu, S.; Nakano, M.; Iwasa, Y. *Adv. Mater.* **2017**, *29*, 1607054.

(14) Le Bideau, J.; Viau, L.; Vioux, A. *Chem. Soc. Rev.* **2011**, *40*, 907−925.

(15) Singh, M. P.; Singh, R. K.; Chandra, S. *Prog. Mater. Sci.* **2014**, *64*, 73−120.

(16) Furukawa, H.; Cordova, K. E.; O'Keeffe, M.; Yaghi, O. M. *Science* **2013**, *341*, 1230444.
(17) Kaskel, S. *The Chemistry of Metal Organic Frameworks: Synthesis, Characterization, and Applications*; Wiley, 2016.
(18) Fujie, K.; Otsubo, K.; Ikeda, R.; Yamada, T.; Kitagawa, H. *Chem. Sci.* **2015**, *6*, 4306−4310.
(19) Kinik, F. P.; Uzun, A.; Keskin, S. *ChemSusChem* **2017**, *10*, 2842−2863.
(20) Leger, J.; Berggren, M.; Carter, S. *Iontronics: Ionic Carriers in Organic Electronic Materials and Devices*; CRC Press, 2011.
(21) Comtet, J.; Nigues, A.; Kaiser, V.; Coasne, B.; Bocquet, L.; Siria, A. *Nat. Mater.* **2017**, *16*, 634−639.
(22) Bermudez, M. D.; Jimenez, A. E.; Sanes, J.; Carrion, F. J. *Molecules* **2009**, *14*, 2888−2908.
(23) Fujie, K.; Yamada, T.; Ikeda, R.; Kitagawa, H. *Angew. Chem., Int. Ed.* **2014**, *53*, 11302−11305.
(24) Chmiola, J.; Yushin, G.; Gogotsi, Y.; Portet, C.; Simon, P.; Taberna, P. L. *Science* **2006**, *313*, 1760−1763.
(25) Merlet, C.; Rotenberg, B.; Madden, P. A.; Taberna, P. L.; Simon, P.; Gogotsi, Y.; Salanne, M. *Nat. Mater.* **2012**, *11*, 306−310.
(26) Futamura, R.; Iiyama, T.; Takasaki, Y.; Gogotsi, Y.; Biggs, M. J.; Salanne, M.; Segalini, J.; Simon, P.; Kaneko, K. *Nat. Mater.* **2017**, *16*, 1225−1232.
(27) Kondrat, S.; Wu, P.; Qiao, R.; Kornyshev, A. A. *Nat. Mater.* **2014**, *13*, 387−393.
(28) Troncoso, J.; Cerdeirina, C. A.; Sanmamed, Y. A.; Romani, L.; Rebelo, L. P. N. *J. Chem. Eng. Data* **2006**, *51*, 1856−1859.
(29) Chui, S. S. Y.; Lo, S. M. F.; Charmant, J. P. H.; Orpen, A. G.; Williams, I. D. *Science* **1999**, *283*, 1148−1150.
(30) Shekhah, O.; Wang, H.; Kowarik, S.; Schreiber, F.; Paulus, M.; Tolan, M.; Sternemann, C.; Evers, F.; Zacher, D.; Fischer, R. A.; Wöll, C. *J. Am. Chem. Soc.* **2007**, *129*, 15118−15119.
(31) Heinke, L.; Tu, M.; Wannapaiboon, S.; Fischer, R. A.; Wöll, C. *Microporous Mesoporous Mater.* **2015**, *216*, 200−215.
(32) Kärger, J.; Ruthven, D. M.; Theodorou, D. N. *Diffusion in Nanoporous Materials*; Wiley VCH, 2012; p 902.
(33) Johannsmann, D. *Phys. Chem. Chem. Phys.* **2008**, *10*, 4516−4534.
(34) Heinke, L.; Gu, Z.; Wöll, C. *Nat. Commun.* **2014**, *5*, 4562.
(35) Liu, J.; Wächter, T.; Irmler, A.; Weidler, P. G.; Gliemann, H.; Pauly, F.; Mugnaini, V.; Zharnikov, M.; Wöll, C. *ACS Appl. Mater. Interfaces* **2015**, *7*, 9824−9830.
(36) Lasia, A. *Electrochemical Impedance Spectroscopy and Its Applications*; Springer, New York, 2014.
(37) Vranes, M.; Zec, N.; Tot, A.; Papovic, S.; Dozic, S.; Gadzuric, S. *J. Chem. Thermodyn.* **2014**, *68*, 98−108.
(38) Delhommelle, J. J.; Cummings, P. T.; Petravic, J. *J. Chem. Phys.* **2005**, *123*, 114505.
(39) Zhao, Y. L.; Dong, K.; Liu, X. M.; Zhang, S. J.; Zhu, J. J.; Wang, J. J. *Mol. Simul.* **2012**, *38*, 172−178.
(40) Shi, J.; Ha, S. D.; Zhou, Y.; Schoofs, F.; Ramanathan, S. *Nat. Commun.* **2013**, *4*, 2676.
(41) Sun, J. Y.; Keplinger, C.; Whitesides, G. M.; Suo, Z. *Adv. Mater.* **2014**, *26*, 7608−7614.
(42) Hurrle, S.; Friebe, S.; Wohlgemuth, J.; Wöll, C.; Caro, J.; Heinke, L. *Chem. Eur. J.* **2017**, *23*, 2294−2298.
(43) Müller, K.; Helfferich, J.; Zhao, F. L.; Verma, R.; Kanj, A. B.; Meded, V.; Bléger, D.; Wenzel, W.; Heinke, L. *Adv. Mater.* **2018**, *30*, 1706551.
(44) Coupry, D. E.; Addicoat, M. A.; Heine, T. *J. Chem. Theory Comput.* **2016**, *12*, 5215−5225.
(45) Boyd, P. G.; Moosavi, S. M.; Witman, M.; Smit, B. *J. Phys. Chem. Lett.* **2017**, *8*, 357−363.
(46) Li, Z.; Xiao, Y.; Xue, W.; Yang, Q.; Zhong, C. *J. Phys. Chem. C* **2015**, *119*, 3674−3683.
(47) Plimpton, S. *J. Comput. Phys.* **1995**, *117*, 1−19.
(48) Hoover, W. G. *Phys. Rev. A: At., Mol., Opt. Phys.* **1985**, *31*, 1695−1697.
(49) Andersen, H. C. *J. Chem. Phys.* **1980**, *72*, 2384−2393.
(50) Sheppard, D.; Terrell, R.; Henkelman, G. *J. Chem. Phys.* **2008**, *128*, 134106.
(51) Miao, J.; Bhatta, R. S.; Reneker, D. H.; Tsige, M.; Taylor, P. L. *Polymer* **2015**, *56*, 482−489.
(52) Xu, W. J.; He, C. T.; Ji, C. M.; Chen, S. L.; Huang, R. K.; Lin, R. B.; Xue, W.; Luo, J. H.; Zhang, W. X.; Chen, X. M. *Adv. Mater.* **2016**, *28*, 5886.